Magicity and occurrence of band with enhanced $B(E2)$ in neutron-rich nuclei ^{68}Ni and ^{90}Zr

K. Kaneko,[1] M. Hasegawa,[2] T. Mizusaki,[3,4] and Y. Sun[5,6,7]
[1]*Department of Physics, Kyushu Sangyo University, Fukuoka 813-8503, Japan*
[2]*Laboratory of Physics, Fukuoka Dental College, Fukuoka 814-0193, Japan*
[3]*Institute of Natural Sciences, Senshu University, Kawasaki, Kanagawa, 214-8580, Japan*
[4]*Center for Nuclear Study (CNS), University of Tokyo, Wako Campus of RIKEN, Wako 351-0198, Japan*
[5]*Department of Physics and Joint Institute for Nuclear Astrophysics, University of Notre Dame, Notre Dame, IN 46556, USA*
[6]*Department of Physics, Tsinghua University, Beijing 100084, P. R. China*
[7]*Department of Physics, Xuzhou Normal University, Xuzhou, Jiangsu 221009, P. R. China*
(Dated: February 9, 2008)

Experimental energy spectrum and B(E2) values in ^{68}Ni and ^{90}Zr indicate a double-magic character in these neutron-rich nuclei with N or $Z = 40$. The data nevertheless do not show any pronounced irregularity in two-nucleon separation energy. To understand the underlying physics, we carry out both shell-model and mean-field calculations. The shell-model calculation can well reproduce all the observations. It is understood from the mean-field results for ^{68}Ni that the shell gap at $N = 40$ disappears due to dynamical correlations of the isovector $J = 0$ pairing interaction. In ^{90}Zr, however, such a dynamic process with the $J = 0$ pairing appears not important because of the strong contribution of the $J > 0$ interaction. We study also level schemes in the Ni isotopes and $N = 50$ isotones. We predict a new band built on the 0_2^+ state in both ^{68}Ni and ^{90}Zr. The states of this band are dominated by two-particle-two-hole excitations from the fp-shell to the intruder $g_{9/2}$ orbit.

PACS numbers: 21.10.Dr, 21.60.Cs, 21.60.Jz, 21.10.Re

arXiv:nucl-th/0607063v2 2 Aug 2006

I. INTRODUCTION

The study of nuclear shell effects away from the valley of stability is one of the current topics in nuclear structure physics. The most interesting aspects are how the well-known shell effects, such as the occurrence of magic numbers [1] and the shape-coexistence phenomenon [2, 3], manifest themselves in exotic mass regions where nuclei have unusual combinations of neutron and proton number. There have been intensive discussions on the issue of weakening of shell effect in neutron-rich nuclei. For example, the spherical $N = 20$ shell gap for light nuclei disappears in neutron-rich isotopes, leading to strongly deformed ground states and large $E2$ transition probabilities between the 2_1^+ state and ground state (0_1^+). By using the shell-model approach, it has been demonstrated [4] that the magic number at $N = 20$ vanishes due to the proton-neutron attraction between spin-orbit partners of maximum j. On the other hand, there have been suggestions [5] that the strong deformation effects around ^{32}Mg are induced by dynamical correlations, such as the neutron pairing correlations.

It has been found [6, 7, 8, 9] by several experiments that the neutron-rich nucleus ^{68}Ni ($Z = 28, N = 40$) shows a double-magic character: a relatively large 2_1^+ excitation energy and a small $B(E2, 0_1^+ \rightarrow 2_1^+)$ value, which is comparable to the cases of double-magic nuclei ^{16}O, ^{40}Ca, and ^{48}Ca. The nucleus ^{68}Ni lies far from the neutron drip line, and the neutron energy gap between the fp-shell and the $g_{9/2}$ intruder orbit appears to be sizeable at $N = 40$. It was discussed in Ref. [10, 11] that in the early mean-field calculations, a distinct shell gap that exists in the $N = 40$ nucleus ^{68}Ni disappears when quadrupole correlations are taken into account. For ^{68}Ni, it is remarkable that this nucleus does not show a pronounced irregularity in two-neutron separation energy, as expected for a typical double-magic nucleus. It was suggested [12] that small $B(E2, 0_1^+ \rightarrow 2_1^+)$ value is not a strong evidence for the double-magic character. We may thus conclude that the double-magicity nature in ^{68}Ni is still controversial and remains an open question.

In general, shell closure leads to spherical configurations for the ground state, while breaking of a magic shell can produce coexisting deformed states. An important indication for the emergent deformation is the appearance of low-lying 0^+ bands. The deformed structure occurs as a consequence of nuclear correlations, which excite nucleons from the closed shell to a higher shell. For example, the typical double-magic nucleus ^{56}Ni ($Z = N = 28$) [13, 14, 15] is known to have two collective bands with large deformations coexisting with the spherical ground band. Therefore, it is very interesting to examine theoretically whether such collective bands exist also in ^{68}Ni.

Similar discussions would also apply to the neutron-rich nucleus ^{90}Zr, which has a closed $Z = 40$ proton subshell and a strong $N = 50$ neutron shell closure. This is an interesting case to study the persistence of the $Z = 40$ stability. Recently, energy levels and $B(E2)$ values in ^{90}Zr have been measured [16], which showed a double magic character: a relatively large 2_1^+ excitation energy and a small $B(E2, 0_1^+ \rightarrow 2_1^+)$ value. However, this nu-

cleus does not indicate a pronounced irregularity in two-proton separation energy. Moreover, it is known that a low-lying 0_2^+ state exists at $Z = 40$ in the $N = 50$ isotonic chain. Hence we can expect to see excited bands in ^{90}Zr but perhaps with different structure.

In this paper, we study the magicity at N or $Z = 40$ and structure of excited 0_2^+ bands in the neutron-rich nuclei ^{68}Ni and ^{90}Zr. To understand the physics in a systematical way, we perform spherical shell-model calculations for the Ni isotopes and $N = 50$ isotones. Conventional shell-model calculations in the $(1f_{7/2}, 2p_{3/2}, 1f_{5/2}, 2p_{1/2}, 1g_{9/2})$ shell space for $N, Z = 30 - 36$ are not possible at present because of the huge dimension of configuration space; we need to restrict the model space to the $2p_{3/2}, 1f_{5/2}, 2p_{1/2}$, and $1g_{9/2}$ orbitals (hereafter called the fpg-shell). Of course, neutron (proton) excitations from the $1f_{7/2}$ orbit to the fpg-shell cannot be neglected for ^{68}Ni (^{90}Zr) [9, 11]. Nevertheless, after all we shall see that the variations in $B(E2)$ in the nuclei around ^{68}Ni (^{90}Zr) can be understood in terms of valence neutrons (protons) in this restricted model space. For the Ni isotopes, we employ an effective interaction starting from a realistic neutron G-matrix interaction based on the Bonn-C NN potential (called VMS interaction) [17]. For the $N = 50$ isotones, we use two types of effective interactions: the proton part of the VMS interaction and the effective interaction of Ji and Wildenthal (called JW interaction) [18].

The paper is arranged as follows. In Sections II and III, we present the numerical calculations and discuss the results for Ni isotopes and $N = 50$ isotones, respectively. Conclusions are drawn in Sec. IV.

II. NI ISOTOPES

A. Magicity in ^{68}Ni

Let us first review what the experiment has found for the Ni isotopes. In Fig. 1, the experimental $B(E2, 0_1^+ \rightarrow 2_1^+)$ value and the first excited 2^+ energy are shown as a function of neutron number N for $^{58-70}$Ni. With increasing N, $B(E2)$ decreases quickly and becomes the smallest at $N = 40$. In contrast, changes in the 2_1^+ energy ($E_{2_1^+}$) are quite small for $^{58-66}$Ni, but $E_{2_1^+}$ jumps to a large value at $N = 40$. Thus, with a pronounced large $E_{2_1^+}$ and a small $B(E2, 0_1^+ \rightarrow 2_1^+)$, these data seem to suggest a subshell closure at $N = 40$ in ^{68}Ni.

We now carry out shell-model calculations for the Ni isotopes. The shell-model Hamiltonian is written as

$$H = \sum_\alpha \varepsilon_\alpha c_\alpha^\dagger c_\alpha + \frac{1}{4} \sum_{\alpha\beta\gamma\delta} V_{\alpha\beta,\gamma\delta} c_\alpha^\dagger c_\beta^\dagger c_\delta c_\gamma, \quad (1)$$

where ε_α are single-particle energies and $V_{\alpha\beta,\gamma\delta}$ two-body matrix elements. Since ^{56}Ni is taken as a core, the model space is restricted to the fpg-shell for neutrons and protons are assumed to be inactive. The proton

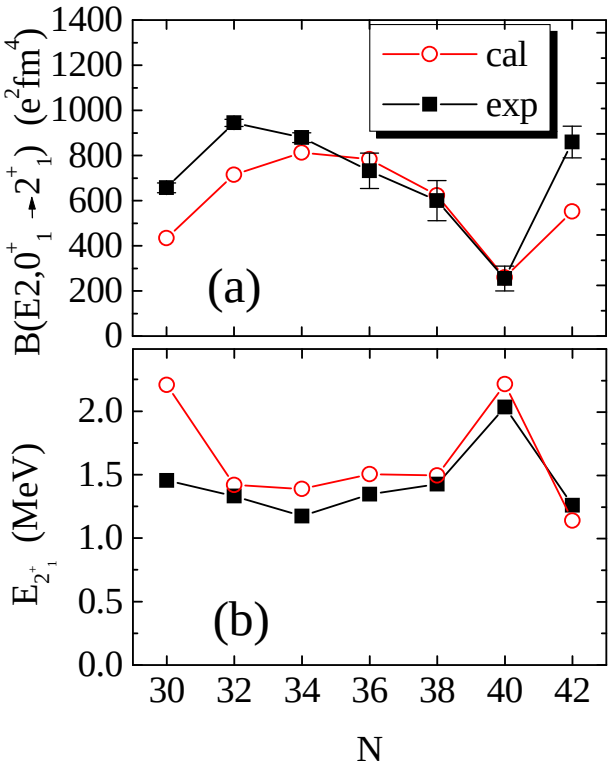

FIG. 1: (Color online) Comparison between the calculated and experimental values of (a) $B(E2, 0_1^+ \rightarrow 2_1^+)$ and (b) $E_{2_1^+}$ for the Ni isotopes. The calculated values are denoted by open circles and the experimental data [6, 9, 19, 20] by solid squares.

core-excitations from ^{56}Ni are taken into account implicitly by the effective two-body matrix elements and the proton contributions are estimated from the KB3 calculations [21] in ^{48}Ca. The neutron effective charge is taken as $e_n = 1.0$ so as to reproduce the experimental $B(E2, 0_1^+ \rightarrow 2_1^+)$ of ^{68}Ni [17]. We use the VMS interaction starting from a realistic neutron G-matrix interaction based on the Bonn-C NN potential.

As one can see in Fig. 1, our calculations reproduce nicely the observed trends in $B(E2, 0_1^+ \rightarrow 2_1^+)$ and $E_{2_1^+}$ [17]. In particular, a large 2_1^+ excitation energy and small $B(E2, 0_1^+ \rightarrow 2_1^+)$ value at $N = 40$ are correctly obtained. It should be pointed out that the proton core excitations may significantly contribute to the excitation energy and to $B(E2, 0_1^+ \rightarrow 2_1^+)$ in ^{58}Ni, and thus it is difficult to absorb these effects into the effective interaction and the effective charges. In addition, the very recent observation [20] indicates a large $B(E2, 0_1^+ \rightarrow 2_1^+)$ value in ^{70}Ni, which exceeds the calculated one. Figure 2 shows two-neutron separation energy S_{2n} and the difference between two-neutron separation energies δ_{2n}, defined respectively by

$$S_{2n}(Z, N) = B(Z, N) - B(Z, N-2), \quad (2)$$
$$\delta_{2n}(Z, N) = S_{2n}(Z, N) - S_{2n}(Z, N+2). \quad (3)$$

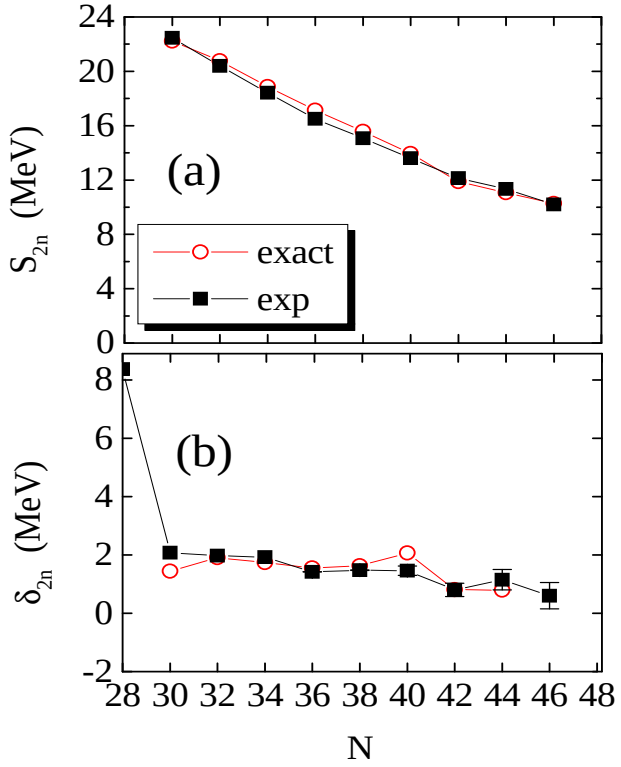

FIG. 2: (Color online) (a) Two-neutron separation energies and (b) differences between the two-neutron separation energies defined in Eq. (3). The exact shell-model results are denoted by open circles and the experimental data [19, 22] by solid squares.

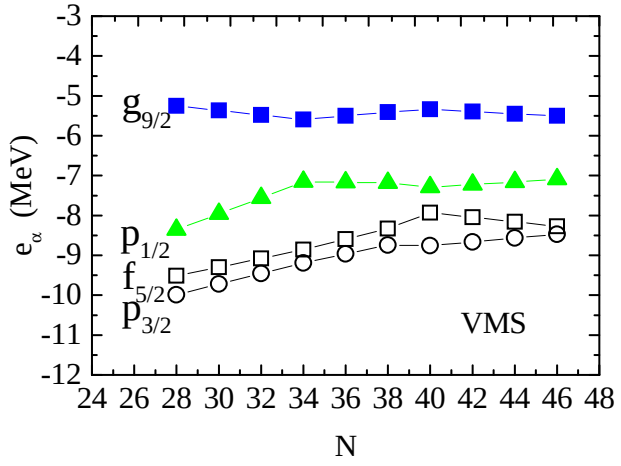

FIG. 3: (Color online) Spherical neutron shell structure. The HF single-particle energy levels e_α predicted in the HF calculations with the VMS interaction for the Ni isotopes.

In Eq. (2), $B(Z,N)$ is the binding energy taken as positive values. The quantity δ_{2n} is known as the most sensitive and direct signature for a (sub)shell closure. Our shell model calculations reproduce well the experimental values of S_{2n} and δ_{2n}. As can be seen in Fig. 2, S_{2n} and δ_{2n} are smooth functions, and in particular, do not show

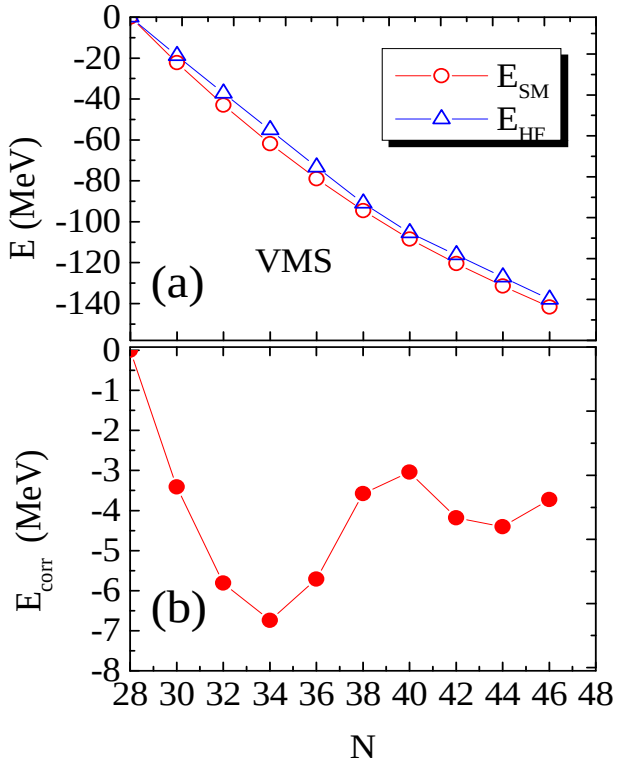

FIG. 4: (Color online)(a) Total energies and (b)correlation energies in the shell-model and the HF calculations with the VMS interaction for the Ni isotopes. Note that the absolute correlation energies become small around $N = 40$.

any notable changes at $N = 40$. Thus, ^{68}Ni has a large $E_{2_1^+}$ and a small $B(E2, 0_1^+ \to 2_1^+)$, but no irregularity in S_{2n} and no strong peak in δ_{2n}. It is therefore very interesting to further look into the S_{2n} and δ_{2n} results from the viewpoint of the magicity in ^{68}Ni.

Let us analyze the shell-model results in Fig. 2 using mean-field procedures. We carry out Hartree-Fock (HF) and Hartree-Fock-Bogolyubov (HFB) calculations using the shell-model Hamiltonian (1). In the calculations, we impose spherical symmetry. The HF single-particle energies are given by

$$e_\alpha = \varepsilon_\alpha + \sum_{\beta=\text{occup}} V_{\alpha\beta,\alpha\beta}, \qquad (4)$$

where $\sum_{\beta=\text{occup}}$ means the summation over the occupied states only. Figure 3 shows the HF single-particle energies e_α. The single-particle energy gap between $g_{9/2}$ and fp-shell varies from 4 MeV at $N = 28$ to 2.5 MeV at $N = 40$, which shows a persistence of a large shell gap at this neutron number. As we shall discuss below, this gap in the static single-particle picture will be washed out by dynamic correlations.

The total HF energy is expressed as

$$E_{\text{HF}} = \sum_\alpha \left(\varepsilon_\alpha + \frac{1}{2} \sum_{\beta=\text{occup}} V_{\alpha\beta,\alpha\beta} \right). \qquad (5)$$

On the other hand, the HFB approximation is carried out with the following procedure. The HFB transformation is given by

$$a^\dagger_\alpha \;=\; u_\alpha c^\dagger_\alpha - v_\alpha c_{\bar\alpha}, \tag{6}$$

where $\bar\alpha$ is the time reversed state to α and the occupation numbers v^2_α satisfy the following equation

$$v^2_\alpha \;=\; \frac{1}{2}\left(1 - \frac{\tilde e_\alpha - \lambda}{\sqrt{(\tilde e_\alpha - \lambda)^2 + \Delta^2_\alpha}}\right). \tag{7}$$

Here the self-consistent mean-fields, the self-consistent pairing gaps, and the canonical single-particle energies are respectively defined as

$$\Gamma_\alpha \;=\; \sum_\beta V_{\alpha\beta,\alpha\beta} v^2_\beta, \tag{8}$$

$$\Delta_\alpha \;=\; \sum_\beta V_{\alpha\bar\alpha,\beta\bar\beta} u_\beta v_\beta, \tag{9}$$

$$\tilde e_\alpha \;=\; \varepsilon_\alpha + \Gamma_\alpha, \tag{10}$$

and the total HFB energy [23] is

$$E_{\rm HFB} \;=\; \sum_\alpha \left[(\varepsilon_\alpha + \frac{1}{2}\Gamma_\alpha)v^2_\alpha - \frac{1}{2}\Delta_\alpha u_\alpha v_\alpha\right]. \tag{11}$$

The neutron chemical potential λ is determined by the neutron number conservation

$$\sum_\alpha v^2_\alpha \;=\; N. \tag{12}$$

Eqs. (7) and (12) are solved iteratively. In this paper, however, we get the solutions by minimizing the total HFB energy (11) with the neutron number conservation (12) under the normalization condition $u^2_\alpha + v^2_\alpha = 1$.

The total shell-model energies $E_{\rm SM}$ and the HF energies $E_{\rm HF}$ are plotted in Fig. 4(a), and the correlation energies, defined as $E_{\rm corr} = E_{\rm SM} - E_{\rm HF}$, are shown in Fig. 4(b). The correlation energy exhibits a characteristic pattern where the absolute value is the largest at $N = 34$ but has a local minimum at $N = 40$. The reduction in correlation energy at $N = 40$ would be attributed to the small pairing gap $\Delta_{1/2}$ of the $p_{1/2}$ orbit with a small j.

Calculations for two-neutron separation energy S_{2n} and the difference between two-neutron separation energies δ_{2n} are shown in Fig. 5. One can clearly see the irregularity in S_{2n} and a peak in δ_{2n} in the HF calculation for ^{68}Ni, which suggest a large energy gap and a subshell closure at $N = 40$. This result is consistent with the most of the Skyrme HF (SHF) and relativistic mean-field (RMF) calculations, which produced a distinct δ_{2n} peak at $N = 40$ [10, 11]. However, as seen in Fig. 5, the irregularity in S_{2n} and peak in δ_{2n} do not show up in the HFB calculations when the $T = 1, J = 0$ pairing interaction is included. We may therefore conclude that

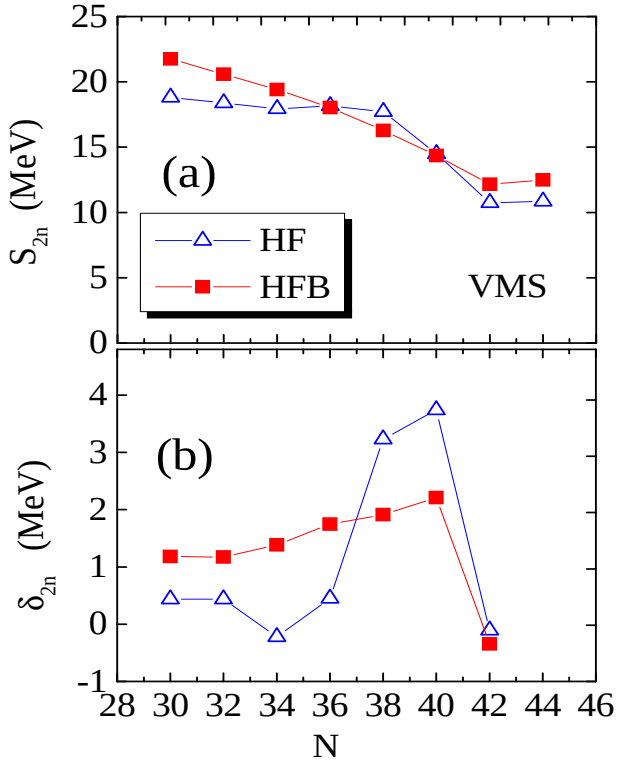

FIG. 5: (Color online) (a) Calculated two-neutron separation energies and (b) differences between the two-neutron separation energies defined by Eq. (3) in the mean-field approximation using the VMS interaction. The HF results are denoted by open triangles and the HFB ones by the solid squares. Note that at $N = 40$ irregularity of S_{2n} appears in the HF calculation and disappears in the HFB calculation.

the $T = 1, J = 0$ pairing interaction is responsible for the observed smooth behavior in S_{2n} and δ_{2n}, and thus for the disappearance of a magicity character in ^{68}Ni. This conclusion is different from that of the SHF and RMF calculations in which the disappearance of the δ_{2n} peak is caused by quadrupole correlations [10, 11].

The above conclusion is reinforced by the following analysis. To see the role of the $T = 1, J = 0$ pairing interaction in the shell model calculations, we divide the two-body interaction H_{int} in the total Hamiltonian (1) into two parts

$$H_{int} \;=\; H_{J=0} + H_{J>0}, \tag{13}$$

where $H_{J=0}$ is the $T = 1, J = 0$ pairing interaction and $H_{J>0} = H - H_{J=0}$. Figure 6 compares different calculations for S_{2n} and δ_{2n}. We evaluate S_{2n} and δ_{2n} by using the binding energy $B(Z, N)$ calculated from the expectation values $\langle H - H_{J=0}\rangle$ and $\langle H - H_{J>0}\rangle$, and compare them with the results of the full Hamiltonian. All these calculations use the same ground-state wavefunction obtained from diagonalization of the total Hamiltonian (1). Now the significant role of the $T = 1, J = 0$ pairing interaction is clearly shown: when $H_{J=0}$ is switched off, S_{2n} exhibits irregularity and a large peak in δ_{2n} is seen

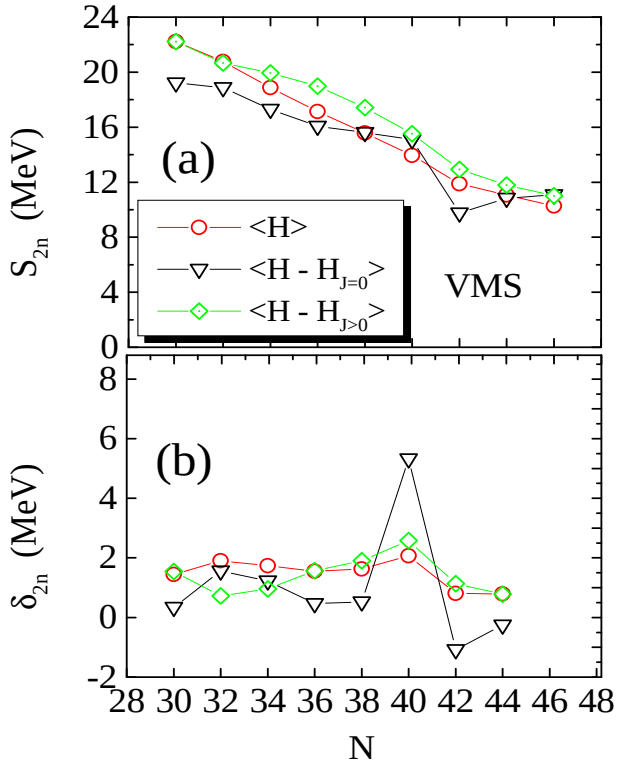

FIG. 6: (Color online) (a) Two-neutron separation energies and (b) differences between the two-neutron separation energies defined by Eq. (3) from the shell-model calculations using the VMS interaction. The exact shell-model results are denoted by open circles, the expectation values neglecting the $T = 1, J = 0$ interactions by open triangles, and the expectation values neglecting the $J > 0$ interactions by open diamonds. Note that only the $\langle H - H_{J=0}\rangle$ result shows irregularity at $N = 40$.

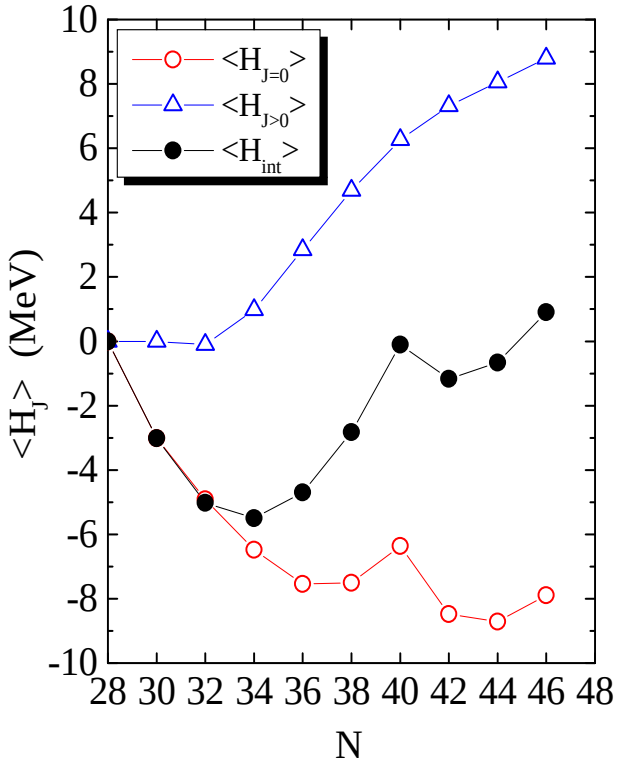

FIG. 7: (Color online) Expectation values of $H_{J=0}$ and $H_{J>0}$ in Eq. (13), which are denoted by open circles and open triangles, respectively. The total interaction energy $\langle H_{int}\rangle$ is also depicted by solid circles. Note that $\langle H_{J=0}\rangle$ displays a bending at $N = 40$.

at $N = 40$, whereas in $\langle H - H_{J>0}\rangle$, no irregularity in S_{2n} and no peak in δ_{2n} can be seen.

In Fig. 7, we further examine the expectation values for various Hamiltonian terms. For the quantity $\langle H_{J=0}\rangle$, one sees that the contribution of the $T = 1, J = 0$ pairing causes a bending at $N = 40$. On the other hand, $\langle H_{J>0}\rangle$ increases monotonously with N. The total expectation value $\langle H_{int}\rangle$ in Fig. 7 corresponds to the correlation energy in Fig. 4 (b). Thus we have understood the source of the seeming irregularity in S_{2n} and the peak in δ_{2n} (see Fig. 5). The irregularity shows up in two-neutron separation energy at $N = 40$ if the $T = 1, J = 0$ pairing interaction is missing. Inclusion of the $T = 1, J = 0$ pairing interaction washes out the irregularities in S_{2n} and δ_{2n} found in the HF calculations, and thus explains the observations. It was inferred from the discussion of the $g_{9/2}$ occupation number that the erosion of the $N = 40$ shell gap is attributed to the pairing correlations [9].

B. Level structure in $^{64-68}$Ni

In this section, we discuss the structure evolution along the isotopic chain $^{64-68}$Ni. Figure 8 shows the experimental and theoretical level schemes. The $B(E2)$ values have been measured only for the first transition between the 2_1^+ state and the ground state [19]. Since in ^{64}Ni, the 0_2^+, 2_2^+, and 4_1^+ states all lie around 2.7 MeV and their excitation energies are approximately twice the first excited 2_1^+ energy (~ 1.38 MeV), the level sequence appears to be consistent with that of an harmonic vibration. This sequence is typical for low-lying excitations in spherical nuclei. Anharmonicity of the 2-phonon states $(0_2^+, 2_2^+, 4_1^+)$ becomes large in ^{66}Ni, and the harmonic pattern breaks down completely in ^{68}Ni where the 0_2^+ level drops down, and appears below the 2_1^+ level.

We carry out shell-model calculations using the VMS interaction. The results are compared with data in Fig. 8 and the predicted $B(E2)$ values are summarized in Table I. The calculations can well reproduce the experimental energy levels and the $B(E2, 0_1^+ \rightarrow 2_1^+)$ values, and the systematic behavior of the low-lying 0_2^+ state is also reasonably described. It is striking that in our results, an excited band is formed in ^{68}Ni based on the 0_2^+ state. The $E2$ transition probability $B(E2, 0_2^+ \rightarrow 2_1^+)$ is quite small in ^{64,66}Ni, but becomes rather large in ^{68}Ni. The

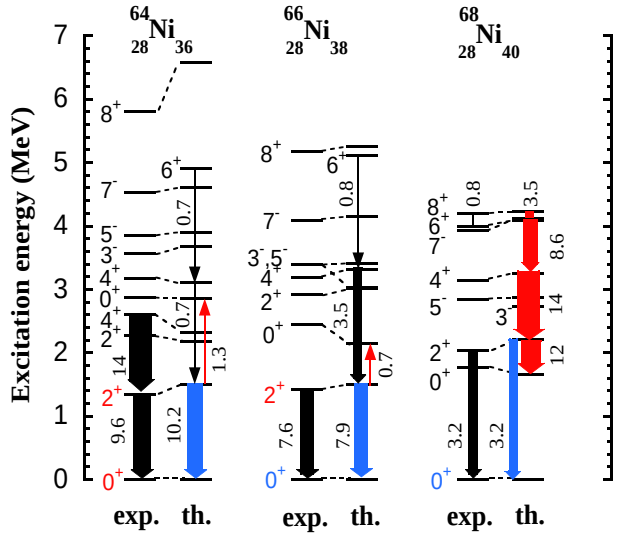

FIG. 8: (Color online) Comparison between the theoretical and experimental level scheme [6, 9, 19] for $^{64-68}$Ni. The widths of the arrows denote relative values of $B(E2)$. The numbers by the arrows are the $B(E2)$ values in Weisskopf units.

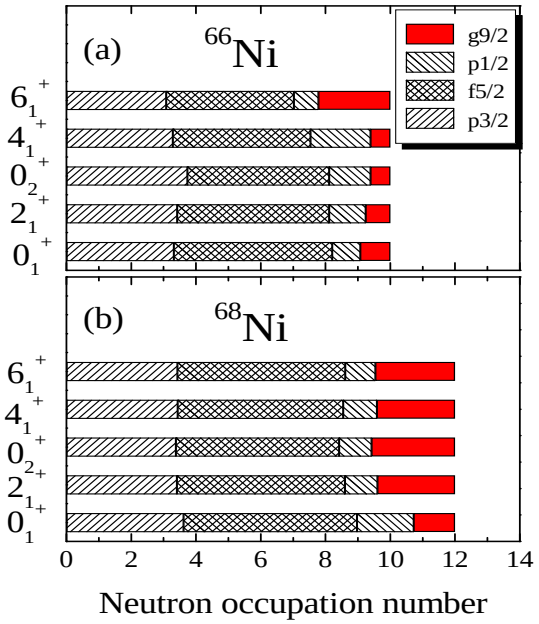

FIG. 9: (Color online) Neutron occupation numbers of the fpg-shell orbits for the low-lying levels in (a) ^{66}Ni and (b) ^{68}Ni.

values $B(E2, 4_1^+ \to 2_1^+)$ and $B(E2, 6_1^+ \to 4_1^+)$ in ^{68}Ni are also large. In contrast, $B(E2, 0_1^+ \to 2_1^+)$ in ^{68}Ni is found smaller than those in ^{64,66}Ni. Thus we have predicted a new band in ^{68}Ni, as shown in Fig. 8.

In order to see how this band is formed, we compare neutron occupation numbers of the $p_{3/2}, f_{5/2}, p_{1/2}$, and $g_{9/2}$ orbits in the relevant low-lying states in ^{66}Ni and ^{68}Ni. As one can see in Fig. 9, except for the 6_1^+ state, neutron occupation numbers in the low-lying states in ^{66}Ni are dominated by the fp-shell components. This is because the Fermi energy of ^{66}Ni lies below the $p_{1/2}$ orbit. However, neutron occupation numbers in ^{68}Ni show very different values [9]. Except for the ground state, occupation number of the $g_{9/2}$ orbit in all low-lying states in ^{68}Ni increases by more than two units. This means that two neutrons are excited from the fp-shell to the $g_{9/2}$ orbit in these states in ^{68}Ni [11, 24]. To see the structure of the low-lying states more clearly, we calculate the probability of n-particle-n-hole (np-nh) excitations from the fp-shell to the $g_{9/2}$ orbit, defined by

$$P_n = \frac{\langle N_n \rangle}{\sum_n \langle N_n \rangle}, \tag{14}$$

where N_n are the np-nh operators from the fp-shell to the $g_{9/2}$ orbit. Table II lists the probabilities of np-nh excitations in the relevant low-lying states of ^{66}Ni and ^{68}Ni. In ^{66}Ni, in all low-lying states except the 6_1^+ state, the dominant components are the 0p-0h excitations but with considerable mixing of the 2p-2h excitations. The 4p-4h excitations are quite small in these states. The 6_1^+ state in ^{66}Ni has almost a pure 2p-2h component. In contrast, the low-lying excited states in ^{68}Ni show very different structures. While the ground state has mixed 2p-2h and 0p-0h components with nearly equal probability, the low-lying excited states have mainly the 2p-2h component with considerable mixing with the 4p-4h excitation. A large $E_{2_1^+}$ and a small $B(E2, 0_1^+ \to 2_1^+)$ in ^{68}Ni (see Fig. 1) would be alternatively explained as follows. Once the odd-parity fp orbits are filled at $N = 40$, at least two-neutrons have to jump to the intruder $g_{9/2}$ orbit to create a 2_1^+ state, and therefore the energy $E_{2_1^+}$ increases [11, 17, 24]. The $E2$ transition between 2_1^+ and 0_1^+ in ^{68}Ni becomes small just because the two states have

TABLE I: $B(E2)$ values for the positive-parity yrast states and some excited states in ^{66}Ni and ^{68}Ni. The calculated values are the shell-model results using the VMS interaction. Data are taken from Refs. [6, 9, 19].

	^{66}Ni [e^2fm^4]		^{68}Ni [e^2fm^4]	
$I_i^\pi \to I_f^\pi$	exp	cal	exp	cal
$2_1^+ \to 0_1^+$	120(20)	125	53(12)	52
$4_1^+ \to 2_1^+$		56		239
$6_1^+ \to 4_1^+$		13		144
$8_1^+ \to 6_1^+$		79	26(1)	58
$2_1^+ \to 0_2^+$		11		198
$2_2^+ \to 0_1^+$		12		15
$2_2^+ \to 2_1^+$		12		36
$2_2^+ \to 0_2^+$		14		27

TABLE II: Probabilities of n particle-hole excitations for the low-lying states of ^{66}Ni and ^{68}Ni.

	^{66}Ni			^{68}Ni		
I^π	0p-0h	2p-2h	4p-4h	0p-0h	2p-2h	4p-4h
0_1^+	0.596	0.347	0.054	0.482	0.405	0.104
2_1^+	0.654	0.311	0.034	0.000	0.728	0.254
0_2^+	0.718	0.260	0.022	0.108	0.610	0.256
4_1^+	0.715	0.262	0.023	0.000	0.800	0.009
6_1^+	0.000	0.891	0.107	0.000	0.779	0.210

different structure. Interestingly, we indeed see from our calculation that the band is built on the 0_2^+ state. This happens because all the excited states belonging to this band have a similar structure with the 2p-2h excitations.

In order to visualize the shape of ^{68}Ni, we use the CHF method with the following quadratic constraint [15]

$$H' = H + \alpha \sum_\mu (\langle Q_{2\mu}\rangle - q_\mu)^2 + \beta(\langle J_x\rangle - j_x)^2, \quad (15)$$

where $Q_{2\mu}$ and J_x are the isoscalar quadrupole operators and the x-component of angular momentum operator, respectively. The q_μ's are constant parameters: $q_0 = \sqrt{\frac{5}{16\pi}} q\cos\gamma$, $q_{\pm 2} = \sqrt{\frac{5}{16\pi}} q\sin\gamma$, and $q_{\pm 1} = 0$, where q is the isoscalar intrinsic quadrupole moment and γ is the triaxial angle. We set $j_x = \sqrt{J(J+1)}$ with J the total angular momentum of the state. The parameters, α and β, are taken so as to achieve a convergence for an iteration calculation with the gradient method. Then, potential energy surface (PES) is defined as the expectation value $\langle H\rangle$ with respect to the CHF state for given q and γ. Figure 10 shows the contour plot of the PES in the q-γ plane for ^{68}Ni. We find that the PES minimum exhibits a spherical shape and an oblate softness. This is consistent with our previous discussions on the shell-model results, namely, a large $E_{2_1^+}$ and a small $B(E2, 0_1^+ \to 2_1^+)$ in ^{68}Ni. The PES figure in Fig. 10 is in contrast to the characteristic feature of an oblate-prolate shape-coexistence in ^{68}Se [25, 26].

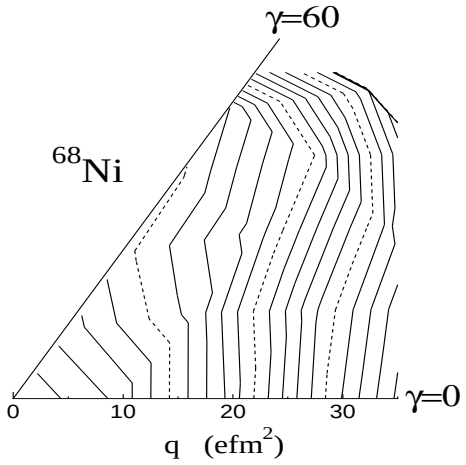

FIG. 10: Contour plot of PES on $q-\gamma$ plane in the CHF calculation for ^{68}Ni.

III. $N = 50$ ISOTONES

A. Magicity in ^{90}Zr

In the previous section, we have discussed several unusual properties found in ^{68}Ni, which are associated with the subshell closure at $N = 40$. A related question is how neutron-rich nuclei with $Z = 40$ behave. Figure 11 shows the experimental $B(E2, 0_1^+ \to 2_1^+)$ and the first excited 2_1^+ energy as a function of proton number Z, for some $N = 50$ isotones. For both $B(E2, 0_1^+ \to 2_1^+)$ and $E_{2_1^+}$ values in Fig. 11, we find remarkable similarities as seen in Fig. 1: with increasing proton number Z, $B(E2)$ quickly increases until $Z = 34$ and then decreases from $Z = 36$ to $Z = 40$. The first excited 2_1^+ energy $E_{2_1^+}$ goes up gradually and is peaked at $Z = 40$. Again, in terms of $B(E2, 0_1^+ \to 2_1^+)$ and $E_{2_1^+}$, ^{90}Zr seems to be a double-magic nucleus. It should be pointed out that $B(E2, 4_1^+ \to 2_1^+)$ shows different behavior from $B(E2, 0_1^+ \to 2_1^+)$ [28]. Recent lifetime measurements for ^{96}Pd and ^{94}Ru corroborate the tendency of this behavior for $N = 50$ [29]. Moreover, it has been shown recently that the exact strengths for these transitions cannot be reproduced in a $T = 1$ model space but require neutron excitations across the $N = 50$ shell [30].

We carry out shell-model calculations for the $N = 50$ isotones. Since ^{78}Ni is taken as a core, the model space for proton is restricted to the fpg-shell, and the neutrons are assumed to be inactive. The proton effective charge is taken as $e_p = 1.8$ for the VMS interaction and $e_p = 2.0$ for the JW interaction so as to reproduce the experimental $B(E2, 0_1^+ \to 2_1^+)$ value of ^{90}Zr [17]. We use two types of effective interactions: the proton part of the VMS interaction and the JW interaction. As one can see in Fig. 11, the calculations nicely reproduce the observed trends for both $B(E2, 0_1^+ \to 2_1^+)$ and $E_{2_1^+}$.

Figure 12 shows the two-proton separation energy S_{2p} and the difference between two-proton separation energies δ_{2p} for this isotonic chain, defined by

$$S_{2p}(Z, N) = B(Z, N) - B(Z-2, N), \quad (16)$$
$$\delta_{2p}(Z, N) = S_{2p}(Z, N) - S_{2p}(Z+2, N). \quad (17)$$

The experimental data do not show a signature for a subshell closure in ^{90}Zr, since no irregularity in S_{2p} can be seen. The shell-model calculations reproduce well the experimental values of S_{2p}. In particular, the small peak in δ_{2p} at $N = 38$ is well described. To understand these results, we analyze the role of the $T = 1, J = 0$ pairing interaction ($H_{J=0}$) and the other interactions ($H_{J>0}$) in the Hamiltonian, as done in the previous section (see Eq. (13)). In contrast to the case of the Ni isotopes,

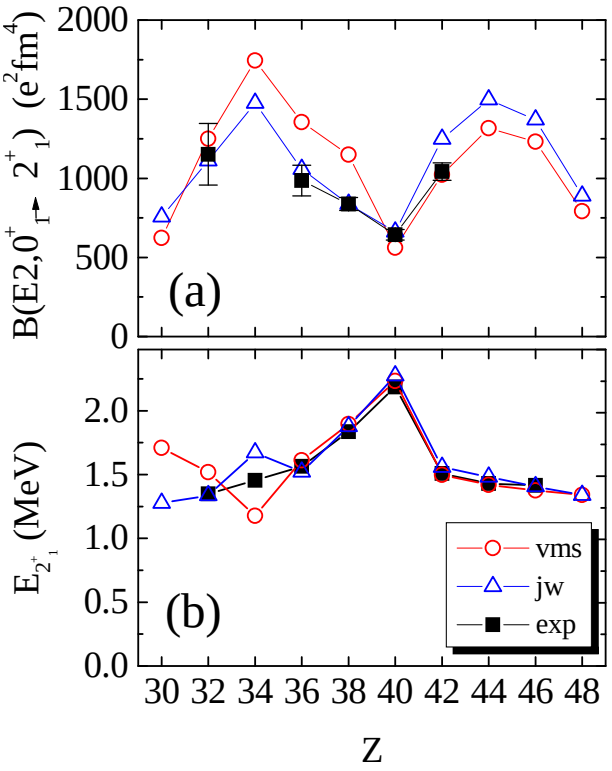

FIG. 11: (Color online) Comparison between the calculated and experimental values of (a) the $B(E2, 0_1^+ \to 2_1^+)$ and (b) $E_{2_1^+}$ for $N = 50$ isotones. Data are taken from Refs. [16, 19, 27]. The shell-model calculations are carried out using the VMS and JW interactions. The calculated results are denoted by open circles (triangles) for the VMS (JW) interaction, and the experimental ones by solid squares.

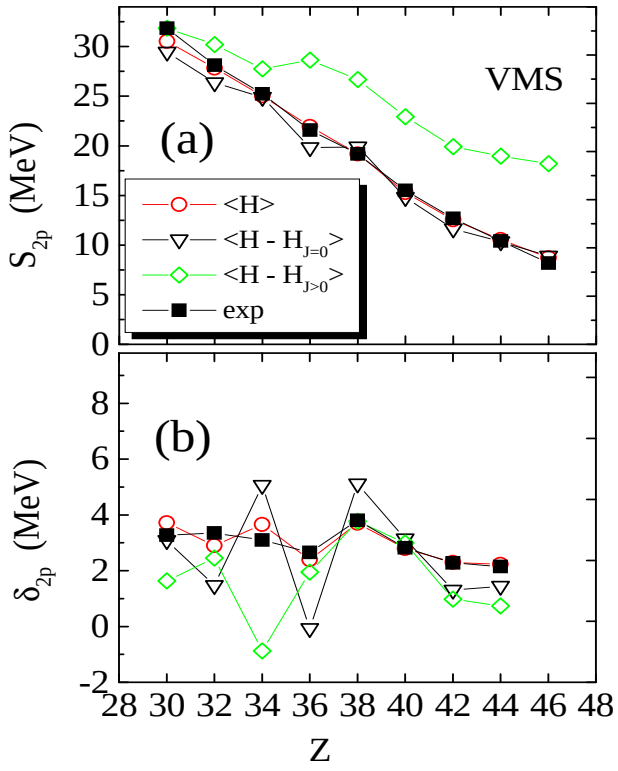

FIG. 12: (Color online) Two-proton separation energies in the shell-model calculations with the VMS interaction. The exact shell model results are denoted by open circles, the expectation values neglecting the $T = 1, J = 0$ interactions by the open triangles, and the expectation values neglecting the $J > 0$ interactions by the open diamonds. Experimental data [19, 22] are denoted by solid squares.

Figs. 12(a) and Fig. 13(a) indicate that, while the $T = 1, J = 0$ pairing interaction scarcely contributes to S_{2p}, the remaining interactions $H_{J>0}$ increases S_{2p} significantly. Thus, the $J > 0$ interactions are more important for two-proton separation energy in the $N = 50$ isotones. The $H_{J>0}$ contribution, however, does not produce any notable irregularity in S_{2p}. For δ_{2p}, we can see some differences between the VMS and JW interactions in Figs. 12(b) and 13(b). Moreover, the $H_{J=0}$ and $H_{J>0}$ contributions to δ_{2p} in the VMS results are different from those in the JW results.

Figure 14 shows the expectation values of $H_{J=0}$, $H_{J>0}$ and the total interaction energy $\langle H_{int}\rangle$. Comparing Fig. 14 with Fig. 7, we find that in the $N = 50$ isotones, $\langle H_{J>0}\rangle$ increases drastically with increasing proton number, and becomes dominant when Z is large. There is no clear bending at $Z = 40$ in either curve $\langle H_{J=0}\rangle$ and $\langle H_{J>0}\rangle$. Thus these detailed results have explained the trends of two-proton separation energy in Fig. 12(a) and Fig. 13(a).

Let us now study the contributions from the above interactions to HF single-particle energies e_α in the HF, HF+BCS, and HFB treatments. We also evaluate two-proton separation energy S_{2p} within these treatments. Figures 15 and 16 show respectively the results calculated with the VMS and JW interactions. It is seen that in the VMS results shown in Fig. 15(a), the single-particle energy gap between $g_{9/2}$ and $p_{1/2}$ orbits decreases quickly with increasing proton number. This causes a smooth variation in S_{2p} as seen in Fig. 15(b). All the HF type calculations do not produce irregularity in S_{2p}. In the JW results in Fig. 16(a), the single-particle energy gap between the $g_{9/2}$ and $p_{1/2}$ orbits remains large up to $Z = 36$, but becomes small after $Z = 38$. The Fermi energy, as found in all HF type calculations, lies in the fp-shell for $Z = 30 - 38$, and between $g_{9/2}$ and $p_{1/2}$ for $Z = 40 - 46$. Therefore, protons do not encounter a large energy gap when they are excited. Therefore, also with the JW interaction, irregularity in S_{2p} is not produced (see Fig. 16(b)). We note that in both Figs. 15 and 16, the proton separation energies in the HFB calculations deviate from those of the other calculations when Z is large. Similar trend is obtained in the shell-model calculation without the $J > 0$ interaction.

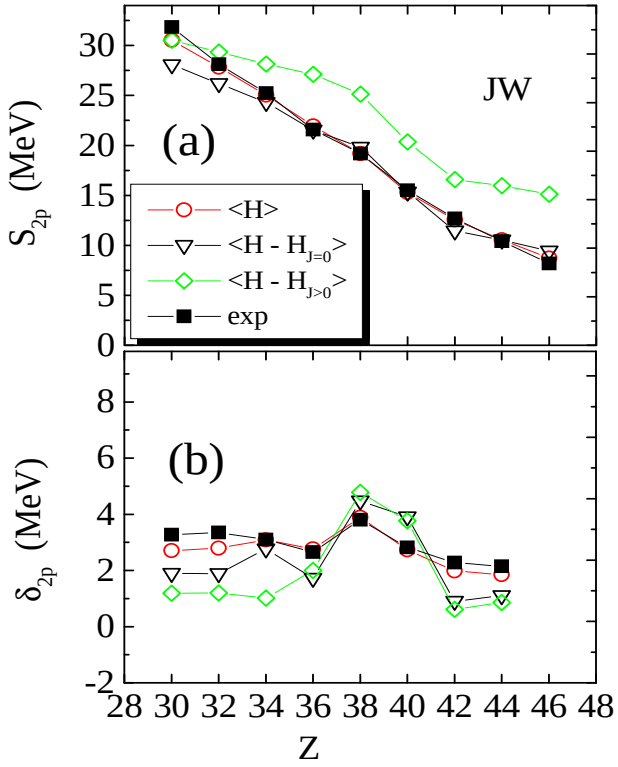

FIG. 13: (Color online) Same as Fig. 12, except that the calculations are performed by using the JW interaction.

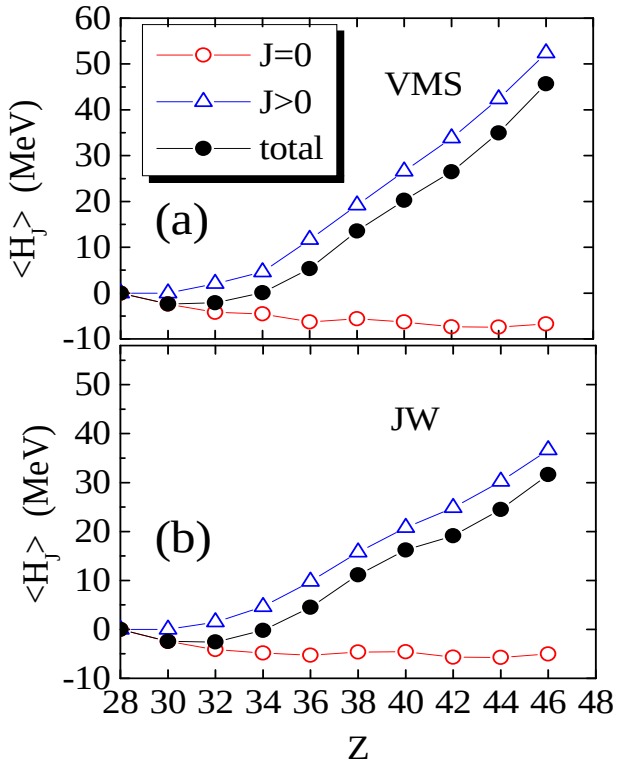

FIG. 14: (Color online) Expectation values of $H_{J=0}$ and $H_{J>0}$ defined by Eq. (13) for (a) the VMS interaction and (b) the JW interaction. $\langle H_{J=0}\rangle$ and $\langle H_{J>0}\rangle$ are denoted by open circles and open triangles, respectively. The total of them ($\langle H_{int}\rangle$) is also depicted by solid circles. Note that the contributions of $\langle H_{J>0}\rangle$ becomes large with increasing proton number.

B. Level structure in ^{86}Kr, ^{88}Sr, and ^{90}Zr

Experimental level schemes for ^{86}Kr, ^{88}Sr, and ^{90}Zr are shown in Figs. 17 and 18. $B(E2)$ in these nuclei has been measured only for transitions between the 2_1^+ state and the ground state. Among the three isotones, the 0_2^+ level in ^{90}Zr is the lowest in energy and lies below the 2_1^+ state. We perform shell-model calculations using the VMS and JW interactions, and the results are compared with data in Figs. 17 and 18 and the $B(E2)$ values are summarized in Tables III and IV.

The calculations can reproduce the experimental energy levels and $B(E2, 0_1^+ \to 2_1^+)$ values. In particular, the systematical behavior of the 0_2^+ state is well described. It is striking that the results show again an excited band in ^{90}Zr based on the 0_2^+ state. For the $E2$ transition probability $B(E2, 0_2^+ \to 2_1^+)$, both calculations indicate a quite small value in ^{86}Kr and ^{88}Sr, but a very large one in ^{90}Zr. Moreover, $B(E2, 4_1^+ \to 2_1^+)$ and $B(E2, 6_1^+ \to 4_1^+)$ are found large in ^{90}Zr. In contrast, $B(E2, 0_1^+ \to 2_1^+)$ in ^{90}Zr is smaller than that in ^{86}Kr and ^{88}Sr. All of these suggest strongly a new band in the $Z = 40$ nucleus ^{90}Zr.

To confirm the above findings, we further study the probability of the np-nh excitations defined by Eq. (14), in two shell-model calculations with the VMS and JW interactions. The results for ^{88}Sr and ^{90}Zr are listed in Tables V and VI, respectively. For ^{88}Sr with the VMS interaction (Table V), the ground state and the 2_1^+ state have a dominant component of the 0p-0h excitation, and the 0_2^+ and 4_1^+ states have comparable probabilities of the 0p-0h and 2p-2h excitations. Note that the 2_1^+ state in

TABLE III: $B(E2)$ values for the positive-parity yrast states and some excited states in ^{88}Sr and ^{90}Zr. Data are taken from Refs. [16, 19]. The calculated values are the shell-model results using the VMS interaction.

	^{88}Sr [e^2fm^4]		^{90}Zr [e^2fm^4]	
$I_i^\pi \to I_f^\pi$	exp	cal	exp	cal
$2_1^+ \to 0_1^+$	167(5)	230	129(4)	112
$4_1^+ \to 2_1^+$		113		277
$6_1^+ \to 4_1^+$		0.2	< 1054	180
$8_1^+ \to 6_1^+$		16	57(4)	65
$2_1^+ \to 0_2^+$		7.3	124(2)	240
$2_2^+ \to 0_1^+$	2.8(1)	0.5		38
$2_2^+ \to 2_1^+$		0.2		38
$2_2^+ \to 0_2^+$		0.1		133

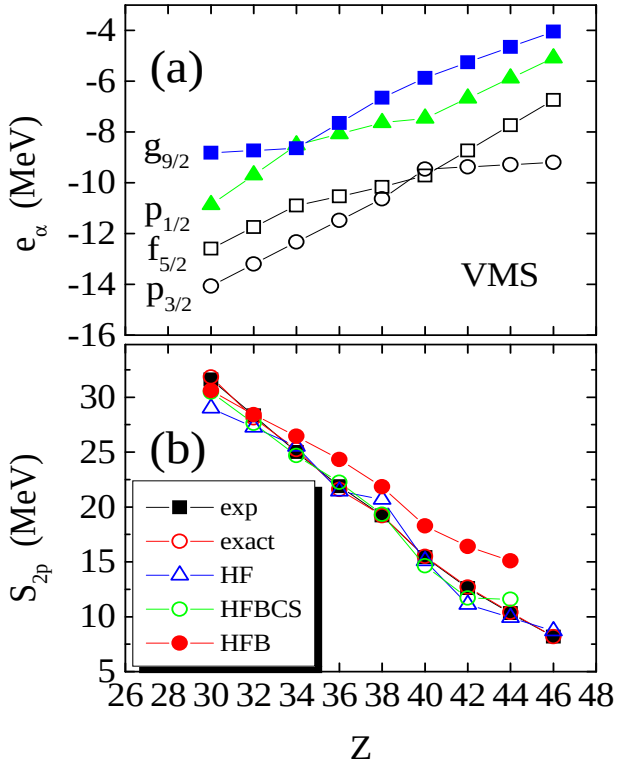

FIG. 15: (Color online) Spherical proton shell structure. (a) The HF single-particle energies e_α obtained by the HF calculations with the VMS interaction and (b) the two-proton separation energies using the mean-field calculations for the $N = 50$ isotones. The HF results are denoted by open triangles and the HFB ones the solid squares.

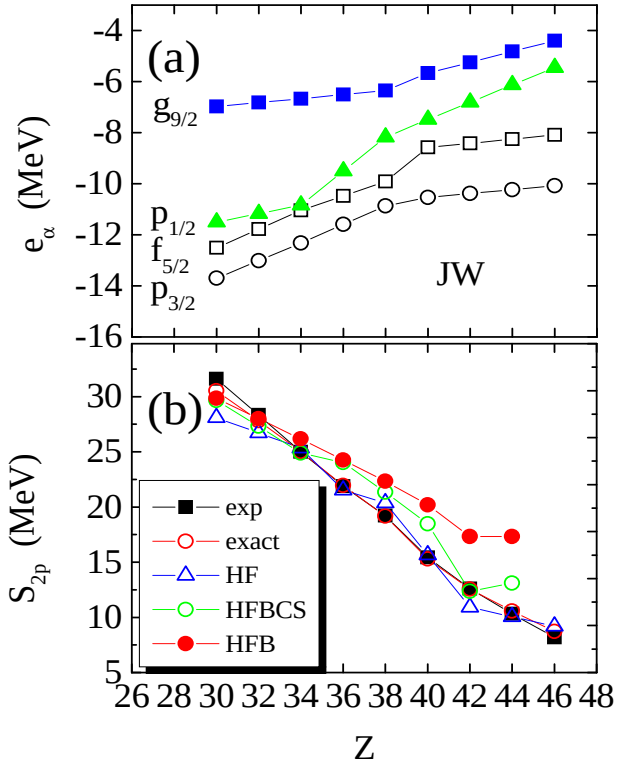

FIG. 16: (Color online) Same as Fig. 15, except that the calculations are performed by using the JW interaction.

^{88}Sr can be made by 1p-1h excitations from $(f_{5/2}, p_{3/2})$ to $p_{1/2}$, which contribute to the $E2$ transitions. In the JW results (Table VI), the 2p-2h components are dominant in the 0_2^+ and 4_1^+ states. The 6_1^+ state is almost a pure 2p-2h excitation in both VMS and JW interactions. One can thus expect that only the $E2$ transition $B(E2, 0_1^+ \to 2_1^+)$ is enhanced in ^{88}Sr. In ^{90}Zr, on the other hand, the ground state has the 0p-0h and 2p-2h components with nearly equal probability and the dominant components in the 2_1^+, 0_2^+, and 6_1^+ states are the 2p-2h excitation

TABLE IV: Same as Table III, except that the calculations are performed by using the JW interaction.

	^{88}Sr [e^2fm^4]		^{90}Zr [e^2fm^4]	
$I_i^\pi \to I_f^\pi$	exp	cal	exp	cal
$2_1^+ \to 0_1^+$	167(5)	166	129(4)	133
$4_1^+ \to 2_1^+$		51		264
$6_1^+ \to 4_1^+$		116	< 1054	192
$8_1^+ \to 6_1^+$		226	57(4)	56
$2_1^+ \to 0_2^+$		70	124(2)	173
$2_2^+ \to 0_1^+$	2.8(1)	117		94
$2_2^+ \to 2_1^+$		23		0.05
$2_2^+ \to 0_2^+$		41		60

TABLE V: Probabilities of np-nh excitations in the low-lying states for ^{88}Sr and ^{90}Zr, where the VMS interaction is used in the shell-model calculations.

	^{88}Sr			^{90}Zr		
I^π	0p-0h	2p-2h	4p-4h	0p-0h	2p-2h	4p-4h
0_1^+	0.732	0.244	0.022	0.425	0.467	0.100
2_1^+	0.799	0.190	0.011	0.000	0.835	0.158
0_2^+	0.498	0.433	0.065	0.300	0.546	0.141
2_2^+	0.811	0.180	0.009	0.000	0.854	0.141
4_1^+	0.496	0.464	0.040	0.000	0.854	0.141
6_1^+	0.000	0.920	0.078	0.000	0.852	0.142

mixed with the 0p-0h component. Similar results are found in both calculations. From this analysis, we can understand that an excited band is formed on the 0_2^+ state in ^{90}Zr because the 0_2^+, 2_1^+, 4_1^+, and 6_1^+ states all have a similar structure with a large component of the 2p-2h excitations.

IV. CONCLUSIONS

We have studied the magicity of N or $Z = 40$ and the level schemes for the neutron-rich nuclei ^{68}Ni and ^{90}Zr by means of the shell-model and the mean-field approximations. For both nuclei with either $N = 40$ or $Z = 40$, their two-nucleon separation energies do not show any irregularity along the respective isotopic or isotonic chain,

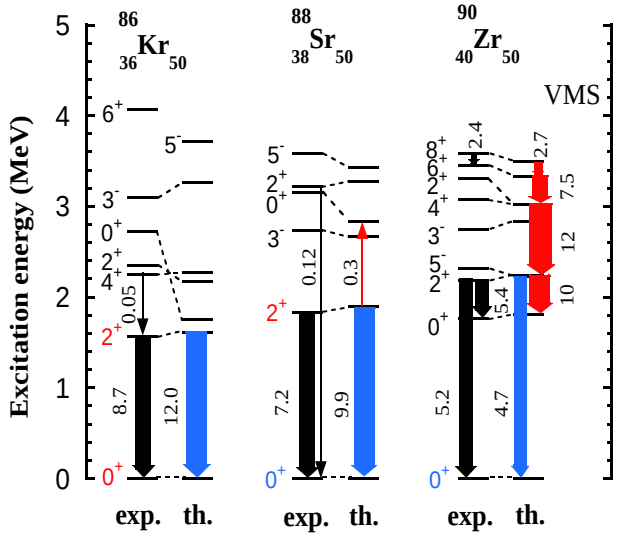

FIG. 17: (Color online) Comparison between the experimental and calculated level scheme for ^{86}Kr, ^{88}Sr, and ^{90}Zr. Data are taken from Refs. [16, 19]. The shell model calculations are carried out by using the VMS interaction. The widths of the arrows denote relative values of B(E2). The numbers by the arrows are the B(E2) values in Weisskopf units.

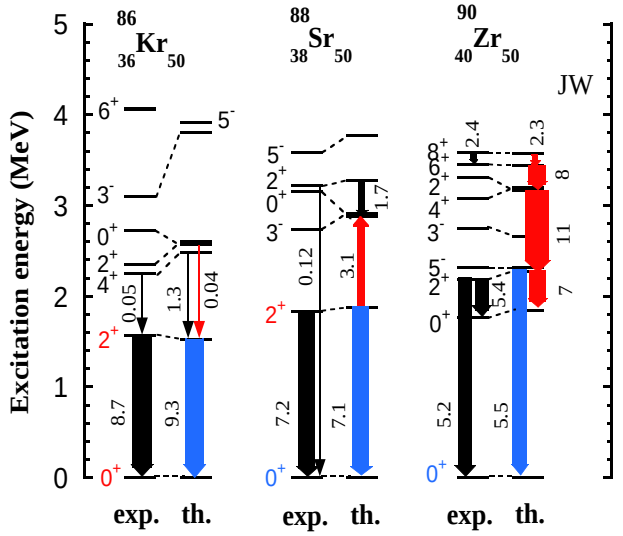

FIG. 18: (Color online) Same as Fig. 17, except that the theoretical results are obtained by using the JW interaction.

in spite of the apparent double-magic feature shown with a comparatively large 2_1^+ excitation energy and a small $B(E2, 0_1^+ \rightarrow 2_1^+)$ value. The reason why the separation energy does not exhibit irregularity has been found different for the Ni isotopes and the $N = 50$ isotones. From the shell-model calculations using the VMS and JW interactions, we have suggested that the $T = 1, J = 0$ pairing interaction is responsible for the absence of any irregularity in separation energy in ^{68}Ni. The irregularity appears in the HF treatment but disappears in the HFB treatment. This indicates that the shell gap at $N = 40$

TABLE VI: Same as Table V, except that the calculations are performed by using the JW interaction.

	^{88}Sr			^{90}Zr		
I^π	0p-0h	2p-2h	4p-4h	0p-0h	2p-2h	4p-4h
0_1^+	0.809	0.184	0.006	0.452	0.484	0.062
2_1^+	0.899	0.100	0.001	0.000	0.894	0.104
0_2^+	0.208	0.729	0.061	0.356	0.523	0.115
2_2^+	0.671	0.320	0.013	0.000	0.925	0.074
4_1^+	0.250	0.714	0.036	0.000	0.904	0.094
6_1^+	0.000	0.967	0.032	0.000	0.912	0.087

disappears due to dynamical correlations of the isovector $J = 0$ pairing interaction. In the case of ^{90}Zr, however, irregularity in two-proton separation energy does not appear in the HF calculations. For the $N = 50$ isotopes, the $J > 0$ interactions contribute significantly to the two-proton separation energy.

We have also studied level schemes for ^{68}Ni and ^{90}Zr. We have predicted an excited band built on the 0_2^+ state in both nuclei. The dominant component of this band has been determined as the 2p-2h excitations from the fp-shell to the intruder $g_{9/2}$ orbit. The structure of the excited states of this band is quite different from that of the ground state. This happens because the opposite signs of parity between the $g_{9/2}$ orbit and the fp-shell do not allow 1p-1h excitations [24]. The first excited 2_1^+ state in ^{68}Ni and ^{90}Zr lies higher, and $B(E2, 0_1^+ \rightarrow 2_1^+)$ is relatively weak. The difference in parity between the fp and the $g_{9/2}$ subshells leads to a small probability of quadrupole excitations across $N = 40$, and the large energy gain due to pairing correlations in the $g_{9/2}$ subshell is responsible for the high 2^+ energy in ^{68}Ni.

[1] M. G. Mayer, Phys. Rev. **75**, 1947 (1949); O. Haxel, J. H. Jensen, and H. E. Suess, Phys. Rev. **75**, 1766 (1949).
[2] K. Heyde, P. Van Isacker, M. Waroquier, J. L. Wood, and R. M. Meyer, Phys. Rep. **102**, 291 (1983).
[3] J. L. Wood, K. Heyde, W. Nazarewicz, M. Huyse, and P. Van Duppen, Phys. Rep. **215**, 101 (1992).
[4] T. Otsuka, R. Fujimoto, Y. Utsuno, B. A. Brown, M. Honma, and T. Mizusaki, Phys. Rev. Lett. **87**, 082502 (2001).
[5] M. Yamagami and N. Van Giai, Phys. Rev. C **69**, 034301 (2004).
[6] R. Broda, *et al.*, Phys. Rev. Lett. **74**, 868 (1995).
[7] R. Grzywacz, *et al.*, Phys. Rev. Lett. **81**, 766 (1998).
[8] T. Ishii, *et al.*, Eur. Phys. J. A **13**, 15 (2002).
[9] O. Sorlin, *et al.*, Phys. Rev. Lett. **88**, 092501 (2002).
[10] P. G. Reinhard, M. Bender, T. Buervenich, C. Reiss, J. Maruhn, and W. Greiner, REKIN Review, **26**, 23 (2000).
[11] H. Grawe and M. Lewitowicz, Nucl. Phys. **A693**, 116 (2001).
[12] K. Langanke, J. Terasaki, F. Nowacki, D. J. Dean, and

W. Nazarewicz, Phys. Rev. C **67**, 044314 (2003).
[13] D. Rudolph, *et al.*, Phys. Rev. Lett. **82**, 3763 (1999).
[14] T. Otsuka, M. Honma, and T. Mizusaki, Phys. Rev. Lett. **81**, 1588 (1998).
[15] T. Mizusaki, T. Otsuka, Y. Utsuno, M. Honma, and T. Sebe, Phys. Rev. C **59**, R1846 (1999).
[16] P. E. Garrett, *et al.*, Phys. Rev. C **68**, 024312 (2003).
[17] A. F. Lisetskiy, B. A. Brown, M. Horoi, and H. Grawe, Phys. Rev. C **70**, 044314 (2004).
[18] X. Ji and B. H. Wildenthal, Phys. Rev. C **37**, 1256 (1988).
[19] R. B. Firestone and V. S. Shirley, *Table of Isotopes*, 8th ed. (Wiley-Interscience, Nwe York, 1996).
[20] O. Perru *et al.*, Phys. Rev. Lett. **96**, 232501 (2006).
[21] E. Caurier, A.P. Zuker, A. Poves, G. Martínez-Pinedo, Phys. Rev. C **50** (1994) 225; A. Poves, A.P. Zuker, Phys. Rep. 70 (1981) 235.
[22] G. Audi and A. H. Wapstra, Nucl, Phys. **A595**, 409 (1995).
[23] P.-G Reinhard, D. J. Dean, W. Nazarewicz, J. Dobaczewski, J. A. Maruhn, and M. R. Strayer, Phys. Rev. C **60**, 014316 (1999).
[24] H. Grawe *et al.*, Proc. TOURS 2000, AIP Conf. Proc., Vol. **561**, 2001, p287.
[25] S. M. Fischer, D. P. Balamuth, P. A. Hausladen, C. J. Lister, M. P. Carpenter, D. Seweryniak, and J. Schwartz, Phys. Rev. Lett. **84**, 4064 (2000).
[26] K. Kaneko, M. Hasegawa and T. Mizusaki, Phys. Rev. C **70**, 051301(R)(2004).
[27] E. Padilla-Rodal *et al.*, Phys. Rev. Lett. **94**, 122501 (2005).
[28] A. Lisetskiy *et al.*, Eur. Phys. J. **A25**, 95 (2005).
[29] H. Mach *et al.*, Proc. Int. Symposium *A New Era of Nuclear Structure Physics*, Niigata, Japan 2003, eds. Y. Suzuki, S. Ohya, M Matsuo, T. Ohtubo, World Scientific, Singapore, 2004, p277.
[30] H. Grawe, A. Blazhev, M. Gorska, R. Grzywacz, H. Mach, and I. Mukha, Eur. Phys. J. **A27**, 257 (2006).